

# The ABCs of Dual-Energy CT

Fides R. Schwartz<sup>1</sup>, Rendon C. Nelson

*Dual-energy CT (DECT), also called multienergy or spectral CT, has been available to diagnostic radiologists since the early 2000s. This innovation was made possible through improvements and progress in CT technology and was based on work originally conducted in the 1970s by Geoffrey Hounsfield [1]. The ability of DECT to improve tissue characterization and assess material composition was first shown in the 1970s [2]. However, at that time, its clinical use was limited by technical factors, such as lengthy CT acquisition times leading to excessive motion artifacts [3], high radiation exposures, and variable tube currents at lower tube voltages compared with higher tube voltages [4].*

DECT requires acquisition of two datasets of the same scan volume with the use of different spectral energy profiles, typically a dataset with a low tube voltage (e.g., 70–100 kVp) and a dataset with a high tube voltage (e.g., 130–150 kVp). As a result, the data profile from every voxel will represent photons from both energy profiles, each of which has a different energy spectrum. With current scanners, this technique can be used to acquire additional information on tissue composition, generate virtual unenhanced images, and improve the conspicuity of iodine attenuation through the generation of iodine maps. From a clinical standpoint, these advances can reduce the number of additional imaging examinations performed to reach a diagnosis (e.g., renal cyst evaluation) or salvage CT examinations with suboptimal contrast enhancement resulting from dosing issues, timing issues, or both [5]. The option to generate virtual monoenergetic datasets from polyenergetic x-ray beams is also advantageous. This is particularly true at lower kiloelectron volt levels (e.g., 40–50 keV), which can substantially improve iodine tissue contrast. An additional advantage of both low- and high-kiloelectron-volt monoenergetic images is the lack of beam-hardening artifacts that are characteristic of polyenergetic x-ray beams [6].

## The As: Atomic Numbers and Other Physics Concepts

To understand the concepts of DECT, it is important to understand how conventional CT works; a single x-ray source and a single x-ray detector are used, and the patient is irradiated with a wide-range of photon energies (polychromatic or polyenergetic beam). The peak energy of the photon is specified by the scan set-

tings (most commonly 120 kVp), but the energy of the photons that interact with the patient's tissue ranges from nearly zero to the peak kiloelectron voltage. The mean incident photon energy from a 120-kVp polyenergetic beam is approximately 60–90 keV on most CT scanners. The optimal tube voltage setting for conventional CT is a compromise between soft-tissue contrast and the level of noise. Low tube voltage settings (e.g., 70 kVp) have high soft-tissue contrast (in particular for substances containing iodine) and a lower radiation dose, but they produce higher levels of noise. High tube voltage settings (e.g., 150 kVp) have a higher radiation dose with lower levels of noise and can penetrate denser tissues such as bone more readily; however, they have reduced soft-tissue contrast (i.e., low contrast detectability).

The concept of DECT includes imaging with two distinctly different energy spectra (e.g., 70 and 150 kVp), either sequentially or simultaneously, to make up for the compromise between tissue contrast and noise while providing additional information regarding tissue composition. The exact scanner setup for acquiring dual-energy datasets with CT equipment from various manufacturers is quite different and will be discussed in a separate chapter [7].

Two basic physics-related principles of the interaction between radiation and matter form the basis of DECT. The first, Compton scattering, is mainly a midenergy phenomenon (inelastic scattering), and the second, the photoelectric effect, is mainly a low-energy phenomenon (Fig. 1).

### Compton Scattering

Compton scattering, the dominant interaction in CT, is dependent on the electron density ( $\rho$ ) and refers to the scattering of an incident x-ray photon by a charged electron in the outermost shell of an atom (the M-shell). Part of the energy of the photon is transferred to the recoiling outer-shell electron, which causes the wavelength of the photon to decrease. At very low energies, this phenomenon is referred to as Thomson scattering and occurs when the incident photon alters neither the kinetic energy level of the charged electron nor the wavelength of the scattered photon.

### The Photoelectric Effect

The photoelectric effect represents a small number of the interactions between x-ray photons and matter in CT, and it mainly comes

<sup>1</sup>Both authors: Department of Radiology, Duke University Medical Center, 2301 Erwin Rd, Box 3808, Durham, NC 27710. Address correspondence to F. R. Schwartz (fides.schwartz@duke.edu).

into play with elements that have a high atomic number, such as iodine, barium, gadolinium, and lead. With this effect, electrons are absorbed rather than scattered. Specifically, an incident x-ray photon that has the proper energy encounters a K-shell electron and ejects it from the atom. This is followed by the cascade of an L-shell electron into the K-shell, which results in the emission of an x-ray photon, which is referred to as the photoelectron [5].

### K-Shell Binding Energy

The K-shell binding energy is unique for each element of the periodic table and increases proportionately to the atomic number. At photon energy levels just higher than the K-shell binding energy, photons are much more likely to be absorbed rather than scattered compared with photons just below the K-shell binding energy, leading to a sudden increase in attenuation, referred to as the k-edge.

The probability of a photoelectric interaction in matter is determined by the K-shell binding energy, which must be approximated by the energy of the incident photon. For example, the binding energy of the K-shell electron in iodine is 33.2 keV. Compared with higher peak kilovoltage polyenergetic x-ray beams, such as 140 kVp, lower peak kilovoltage beams, such as 80 kVp, consist of a much higher percentage of x-ray photons with an energy approximating 33.2 keV, which results in a much higher percentage of photoelectric interactions and, hence, the higher attenuation of iodine. For organic matter such as a carbon, oxygen, and nitrogen, which are the most plentiful atoms in the body, the k-edge is so low (< 10 keV) that there essentially are no photoelectric interactions with x-rays beams ranging from 70 to 150 kVp. Because the k-edge is linked to the atomic number, it makes it possible to derive information about an element from the degree of attenuation observed at different energy levels (Table 1). Observing the attenuation of an element at two distinct energy levels (e.g., by using two different peak kilovoltages for the acquisition of a CT dataset) can help differentiate between two elements, if there is a sufficient difference in the k-edges. This is commonly referred to as spectral separation based on the CT number ratio (Fig. 2). Metals commonly used in or-

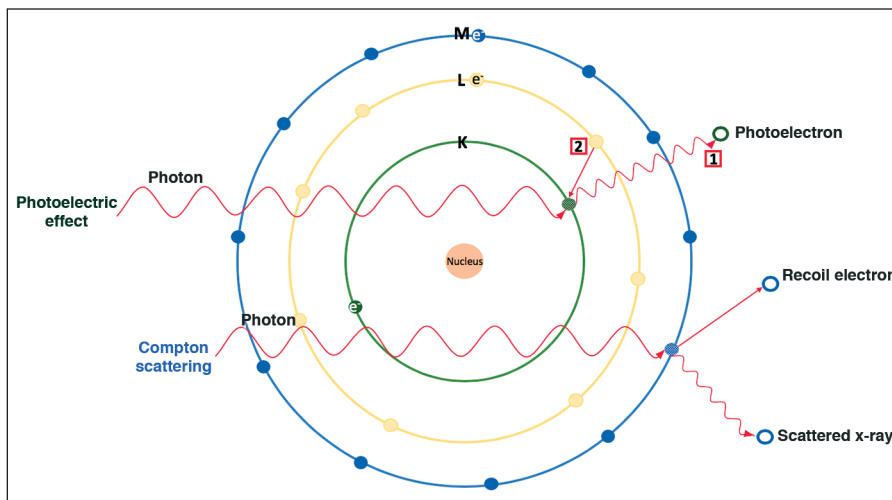


**Fig. 1**—Diagram showing most common effects of electromagnetic radiation from CT, including Compton scattering and photoelectric effect. Photoelectron (denoted by “1”) emitted via photoelectric effect has energy different from that of incidental photon that collided with electron from K-shell (denoted by “K”), dislodging it in process. Electron (denoted by “2”) from L-shell (denoted by “L”) fills K-shell after photoelectron has been emitted. Compton scattering occurs at higher energy level than photoelectric effect and leads to scattered x-ray photon with part of energy transferred into recoiling electron. Solid arrows show movement of electrons from one shell to another and out of their shell respectively; curved arrows show movement of photons or x-ray scatterer.

**TABLE 1: Common Human Body Composition Elements and Contrast Media With Characteristics Important for Dual-Energy Imaging**

Element	Atomic Number (Z)	k-Edge
Hydrogen	1	0.01
Carbon	6	0.28
Nitrogen	7	0.4
Oxygen	8	0.53
Calcium	20	4.0
Titanium	22	4.97
Iodine	53	33.2
Barium	56	37.45
Gadolinium	64	50.2
Lead	82	88.01

thopedic implants, such as titanium and cobalt-chromium alloys, have similar k-edges, so separation is not currently useful.

### Outcomes: Different Image Types

Depending on the acquisition method, postprocessing can be performed either in the projection domain (using raw data from the scanner) or in the image or slice domain. With use of these datasets, it is possible to reconstruct three different types of images.

The first type consists of images that appear similar to standard CT images acquired

at 120 kVp and can be used for routine clinical interpretation. These images are often referred to as mixed or combined images, and they are achieved by the linear blending of data from the two different peak kilovoltage acquisitions, whether they are acquired via rapid-kV-switching, dual-source technology, or dual-layer technology [8].

The second type consists of virtual monoenergetic images (VMIs), which simulate the images that could be acquired with a true monoenergetic x-ray source [6]. Instead of the polyenergetic x-ray beam,

which has a wide range of photon energies that culminate in the peak kilovoltage, these virtual monoenergetic x-ray beams consist of photons with a similar energy expressed as kiloelectron volts (Table 2). VMIs reconstructed at 75 keV are considered approximately equivalent in appearance to conventional images acquired at 120 kVp. The advantages of VMIs, however, are that the images can have a lower level of noise depending on the algorithm used and that they do not yield beam-hardening artifacts. Exploiting the principle of k-edge imaging, low-energy VMIs reconstructed close to the k-edge of iodine at 33.2 keV show substantially higher attenuation of structures containing iodine and can be used to optimize enhancement of hypervascular lesions and parenchyma as well as blood vessels [9] (Table 3). Conversely, high-energy VMIs can be used to reduce aliasing or streak artifacts caused by metallic implants or high-density contrast material as well as blooming artifacts caused by calcium [10].

The third type consists of material decomposition images created from the dual-energy dataset. The most commonly used image pair is water and iodine (i.e., water only and iodine only), which can be understood as mirror images of each other. After an iodine map is generated, it becomes possible to subtract that data and produce virtual unenhanced images. Iodine maps are created by taking advantage of the distinctly different k-edges of water and iodine, which are close to 0 and 33.2 keV, respectively, and they can then be displayed for qualitative assessment either in gray scale (allowing iodine concentration measurements validated in phantom studies) or as a color overlay on anatomic images [11].

### The Bs: Bones, Vessels, Tumors, and Other Applications Musculoskeletal Applications

In musculoskeletal imaging, high-energy virtual monoenergetic imaging is useful for reducing aliasing or streak artifacts from metallic implants (e.g., spinal reconstruction or arthroplasties), thereby improving detectability of loosening screws or processes adjacent to the implant, like abscesses [10] (Fig. 3).

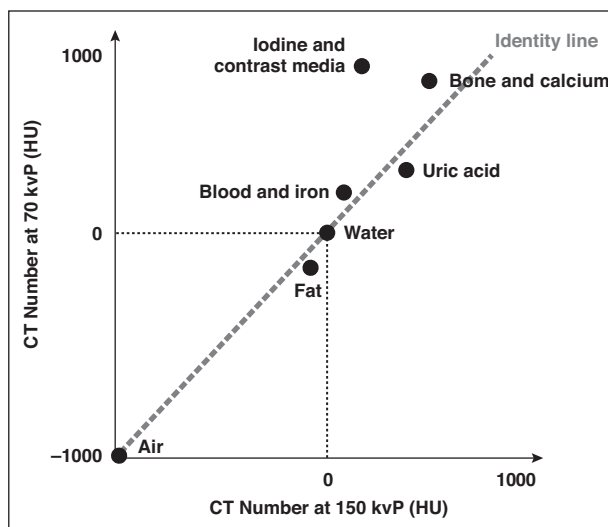


**Fig. 2**—Graph shows principle of material decomposition. CT numbers of typically encountered materials from low- and high-energy images are plotted along y- and x-axes. Identity line or line of equality (*dashed line*) has slope of 1 and shows values at which both CT numbers are same. In human body, air (−1000 HU) and water (0 HU) are relevant materials along this line. Elements that are further apart are shown on this graph; it is easier to separate them via dual-energy imaging with material decomposition. Dotted lines denote visual cue or reminder that water = 0 HU in either monoenergetic spectrum.

**TABLE 2: Ideal Kiloelectron Volt Values for Virtual Monoenergetic Image (VMI) Reconstructions, Depending on the Structure Imaged or the Suspected Pathology**

Structure Imaged	Ideal Kiloelectron Volt Value(s) for VMI
Vessels	40–60
Pancreas	50
Gallstones	40
Metallic implants	108–149

**TABLE 3: Iodine Threshold Cutoff Values for Distinguishing Pathologies From Their Harmless Counterparts**

Suspected Pathology	Iodine Threshold Cutoff (mg/mL)
Thrombus in left atrial appendage	1.74
Malignant mediastinal mass	1.58
Enhancing renal lesion [1]	0.5
Neoplastic thrombus	0.9

CT arthrography can profit from iodine maps. An example of this is the ability to distinguish contrast material penetrating through a labral or rotator cuff tear from calcified structures [12].

Arguably, the most commonly used diagnostic tool in musculoskeletal imaging is material decomposition imaging of uric acid to identify gout crystals, especially for patients with atypical clinical presentations [13] (Fig. 4).

Bone marrow edema can be quantified using material decomposition images that separate out calcium; this can be helpful in the diagnosis of acute conditions (e.g., fractures) and chronic processes (e.g., axial spondyloarthritis) [14] as well as for oncologic applications (e.g., evaluation of

multiple myeloma) [15]. In addition, ligaments and tendons can be highlighted with material decomposition images because of their distinctive collagen content, with collagen side chains being composed of densely packed hydroxyproline and hydroxylysine so they can be separated from water and calcium in the surrounding muscles and bones [16].

### Vascular and Cardiac Applications

As previously mentioned, VMIs can be used to optimize contrast enhancement of blood vessels. This is especially helpful for improving enhancement in patients with renal insufficiency, who may receive a reduced dose of contrast material. It may also be a tool for improving

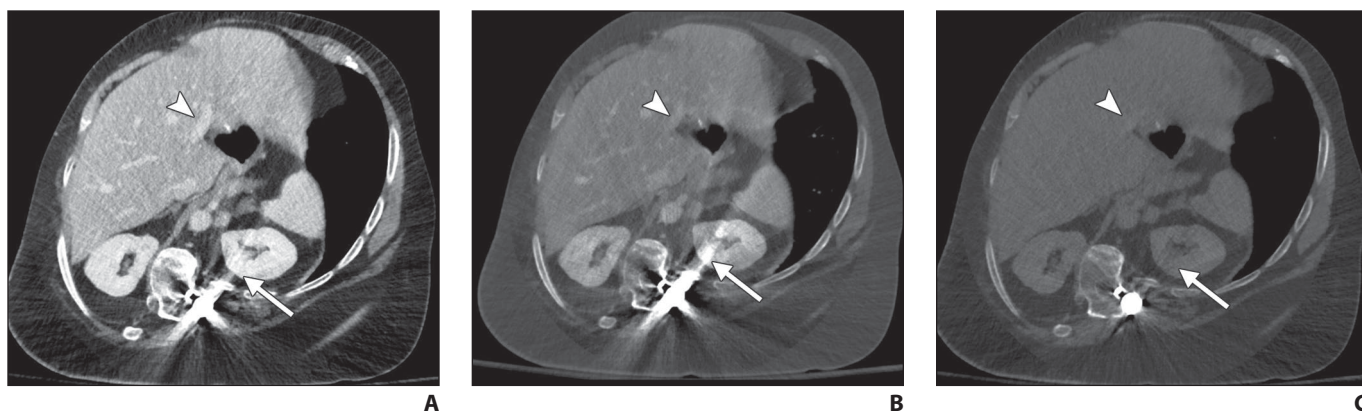


**Fig. 3**—Portal venous phase abdominal CT images obtained after spinal reconstruction surgery. **A**, Normal blended image shows considerable amount of metal artifact (*arrow*) overlaying left kidney and good contrast in portal veins (*arrowhead*). **B**, Virtual monoenergetic image of same slice shown in **A**, obtained at 50 keV, shows high portal venous contrast (*arrowhead*) and high amounts of metal artifact (*arrow*). **C**, Virtual monoenergetic image of same slice shown in **A**, obtained at 150 keV, reveals decreasing amounts of metal artifact (*arrow*) and loss of portal venous contrast (*arrowhead*).

depiction of the vascular system in patients with suboptimal vascular contrast resulting from large habitus or in children with low-radiation-dose acquisitions [6]. Furthermore, it can enable low contrast media dose imaging for complex preprocedural planning such as transaortic valve replacement, evaluation of aortic abnormalities [17], and vascular structures with a complex physiologic enhancement profile, such as the portal veins [18].

Virtual unenhanced images can be helpful in acute vascular emergencies, an example of which is patients undergoing evaluation for aortic dissection where unenhanced images are needed to assess for intramural hematomas. Furthermore, for cases in which a dissection is not clinically suspected but is seen on contrast-enhanced images, virtual unenhanced images can show an intramural hematoma without the need for additional CT [19]. Visualization of suspected hemorrhage, such as in the gastrointestinal tract, is another application of virtual unenhanced imaging used in combination with iodine maps. Specifically, virtual unenhanced images may confirm or improve confidence in determining whether a hyperattenuated focus seen in the bowel lumen on contrast-enhanced images is a solid, enhancing mass or ingested material. When a hyperattenuated lesion is identified on virtual unenhanced images, such as in the liver or brain, the iodine map may assist in detecting active extravasation of contrast material [20]. In addition,



**Fig. 4**—Patient with suspected tophus of first interphalangeal joint caused by gout. **A**, Mixed CT image that is equivalent to single-energy scan acquired at 120 kVp shows tophus (*arrowhead*). **B**, Material decomposition image applied to highlight urate crystals (*green area* indicated by *arrowhead*) confirms that lesion seen on regular CT scan is tophus caused by gout.

the critical diagnosis of acute bowel ischemia may be improved by showing decreased enhancement in the bowel wall on iodine maps [21].

For the thorax, iodine map–based images can be used to combine vascular analysis with functional assessment of parenchymal enhancement, which can help visualize the

pulmonary perfusion, highlight pulmonary emboli, and show the changes caused by pulmonary hypertension [22] (Fig. 5).

Several uses for DECT exist in cardiac imaging, including reducing metal artifacts via virtual monoenergetic imaging [23, 24], providing information on cardiac perfusion via iodine map evaluation [25],

and enabling atherosclerotic plaque analysis via material decomposition [26].

**Oncologic Imaging Applications**

Low-energy VMIs can be used to increase lesion conspicuity, especially in hypervascular lesions in the liver and pancreas, such as hepatocellular carcinoma and pan-

creatic neuroendocrine tumors, respectively [27, 28] (Fig. 6). Alternatively, it may be helpful for detecting hypoenhancing tumors that occur in organs that typically show parenchymal hyperenhancement, such as pancreatic ductal adenocarcinomas.

Virtual unenhanced images and iodine maps can be used to evaluate renal and oth-

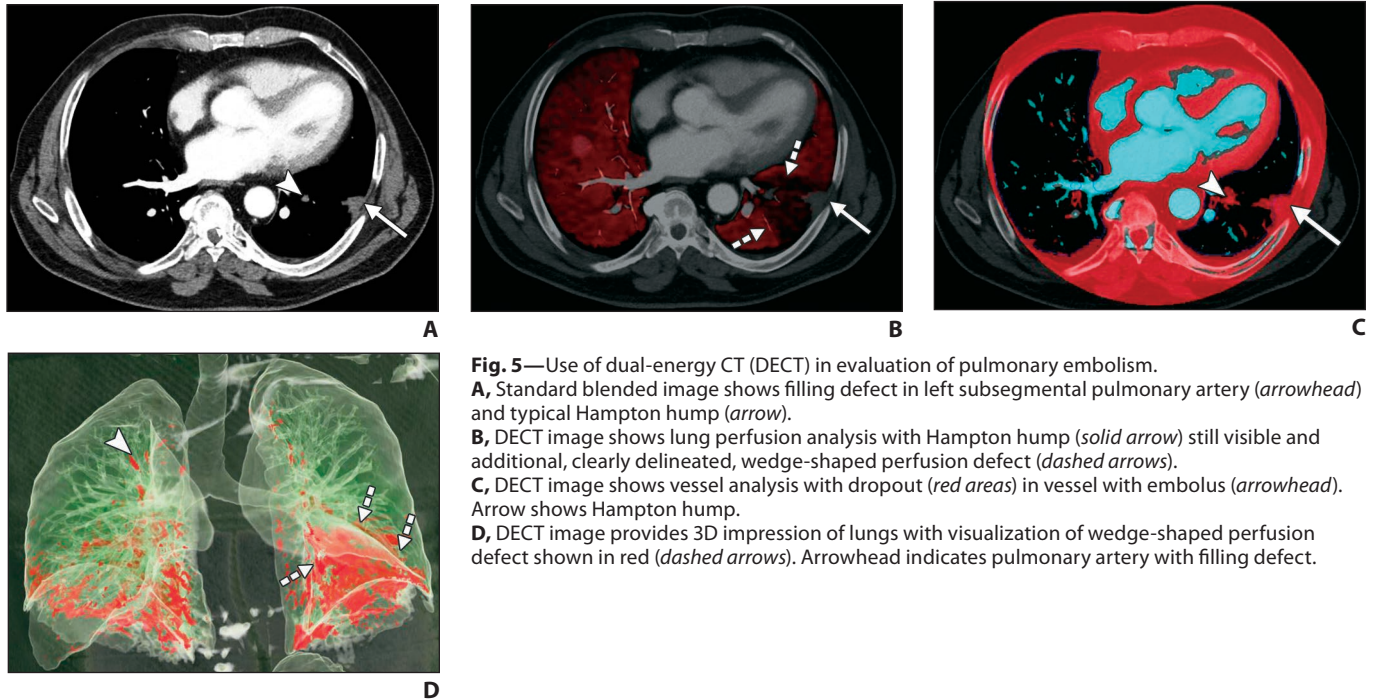


**Fig. 5**—Use of dual-energy CT (DECT) in evaluation of pulmonary embolism. **A**, Standard blended image shows filling defect in left subsegmental pulmonary artery (arrowhead) and typical Hampton hump (arrow). **B**, DECT image shows lung perfusion analysis with Hampton hump (solid arrow) still visible and additional, clearly delineated, wedge-shaped perfusion defect (dashed arrows). **C**, DECT image shows vessel analysis with dropout (red areas) in vessel with embolus (arrowhead). Arrow shows Hampton hump. **D**, DECT image provides 3D impression of lungs with visualization of wedge-shaped perfusion defect shown in red (dashed arrows). Arrowhead indicates pulmonary artery with filling defect.

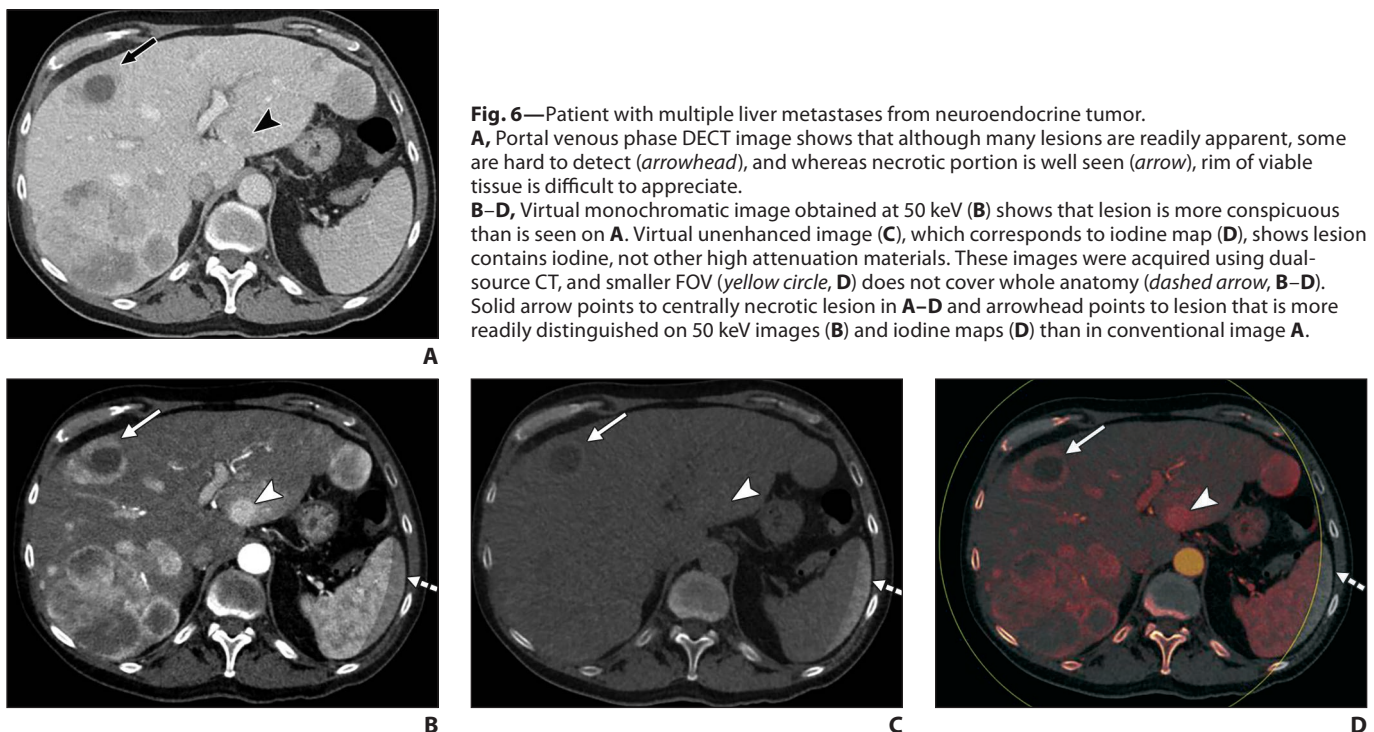


**Fig. 6**—Patient with multiple liver metastases from neuroendocrine tumor. **A**, Portal venous phase DECT image shows that although many lesions are readily apparent, some are hard to detect (arrowhead), and whereas necrotic portion is well seen (arrow), rim of viable tissue is difficult to appreciate. **B–D**, Virtual monoenergetic image obtained at 50 keV (**B**) shows that lesion is more conspicuous than is seen on **A**. Virtual unenhanced image (**C**), which corresponds to iodine map (**D**), shows lesion contains iodine, not other high attenuation materials. These images were acquired using dual-source CT, and smaller FOV (yellow circle, **D**) does not cover whole anatomy (dashed arrow, **B–D**). Solid arrow points to centrally necrotic lesion in **A–D** and arrowhead points to lesion that is more readily distinguished on 50 keV images (**B**) and iodine maps (**D**) than in conventional image **A**.

er cystic lesions [29]. Virtual unenhanced images may be used to characterize hyperattenuated lesions that might otherwise have to undergo additional unenhanced CT or MRI for confirmation of a hemorrhagic cyst. Conversely, iodine maps can confirm the presence of contrast material in a hyperattenuated renal lesion, increasing the likelihood of a malignant tumor and enabling a more confident recommendation for a biopsy, an ablation, or excision. A similar approach can be taken regarding adrenal incidentalomas and ovarian cysts [30] (Fig. 7).

### Other Applications

Low-energy VMIs can be helpful in evaluating mural integrity in the bowel and urinary bladder as well as for increasing the conspicuity of isoattenuating gallstones [31, 32].

Inflammatory bowel conditions can be evaluated using virtual unenhanced images and iodine maps when a significantly increased iodine concentration in the bowel wall suggests active inflammation compared with normal bowel [21].

Renal calculi can be identified and classified using material decomposition imaging based on the attenuation values obtained for uric acid and calcium [33] (Fig. 8).

Iron content can be mapped via material decomposition to determine iron overload in the liver [34] and myocardium [35] as well as pigmented villonodular synovitis, hemophilic arthropathy, and hemochromatosis arthropathy [36].

An emerging application for DECT exists in CT colonography in which tagged fecal material can provide artifact-free visualization of the colonic lumen and mate-

rial decomposition can be used to remove artifact caused by the cleansing agent [37].

### The Cs: Challenges

#### Organ Systems

In musculoskeletal imaging, special care needs to be taken when positioning the patient; when imaging gout crystals, the examined extremity should not be placed alongside the body or the head because this can introduce artifacts through beam hardening [38]. Nail beds and skin calluses can also mimic urate deposits, but they usually are easily ruled out by taking note of the location or by inspection of the standard gray-scale images [39]. Analysis of fractures can be challenging in sclerotic regions, such as in degenerative disease or at the bony cortex, thus making small avulsion fractures difficult to assess.

Although evaluation of fat and iron content in the liver is a valid application of DECT, such evaluation is complicated if both fat and iron are present [40]. The representation of tissue containing fat generally is dependent on the amount of beam hardening that occurs in the body, so it can vary in accuracy [41].

Diffuse bone marrow infiltration in multiple myeloma is difficult to assess with DECT, and lesion vitality may not be assessable with calcium subtraction algorithms [15]. Only yellow bone marrow can be imaged well, because its CT numbers are sufficiently different from those of calcium (CT number of 20 vs 33); red bone marrow cannot be visualized well. This can make marrow evaluation in the vertebrae of younger patients unreliable [42].

The distinction between the blood vessel lumen and calcified plaque is impor-

tant in the evaluation of small vessels in the heart (as in coronary artery disease) as well as in the lower extremities (as in peripheral artery disease). However, because the k-edges of iodine and calcium are relatively similar, the small vessel diameter, the presence of motion (particularly of the coronary arteries), or a combination of these two findings makes this a difficult application for DECT [43].

#### Acquisition Systems

Some DECT acquisition methods, such as dual-source CT, are more susceptible to motion artifacts than others. This can be especially challenging for cardiac and pulmonary applications because temporal resolution is the key to identifying coronary artery stenoses, cardiac valvular disease, and pulmonary emboli in small, peripheral veins [22, 44]. Another challenge in dual-source systems is the fact that dual-energy information is available only for a limited FOV diameter of 33 cm or 35 cm because of the reduced size of the second detector, thereby emphasizing the importance of centering the patient.

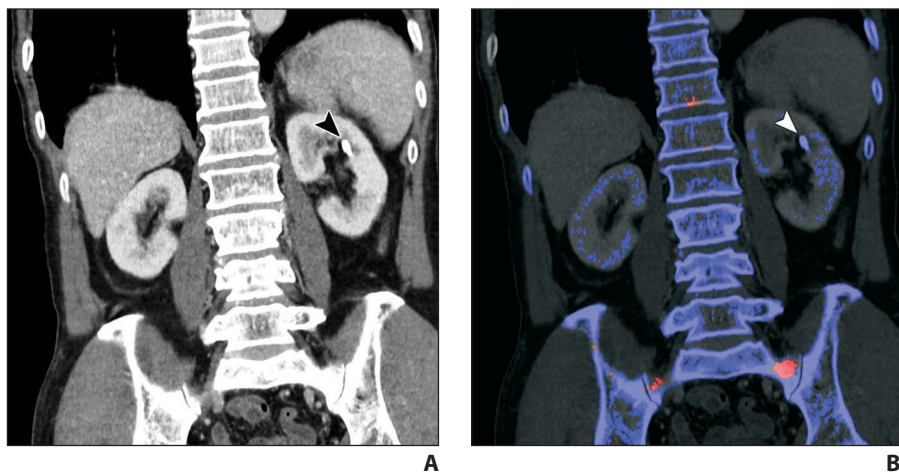
Although not as vulnerable to motion artifacts, rapid kilovoltage switching and dual-layer detector-based DECT systems have lower dual-energy resolution than dual-source systems and therefore may require radiation doses that are higher than those used in single-energy imaging [45].

Image noise is a problem for all DECT systems. One way to improve image quality is to perform image blending in which images are reconstructed from different amounts (typically 50%) of data from the two energy levels, resulting in noise similar to that of a single-energy acquisition at



**Fig. 7**—Patient with multiple ovarian cysts.

**A**, Blended dual-energy CT image shows that one cyst (*arrowhead*) is diffusely hyperattenuated **B** and **C**, Virtual unenhanced image (**B**) shows slightly hyperattenuated interior of cyst (*arrowhead*), and iodine map (**C**) shows no contrast material inside cyst (*arrowhead*), enabling confident diagnosis of hemorrhagic cyst.



**Fig. 8**—Evaluation of renal calculus with dual-energy CT. **A**, Blended image clearly shows calculus (arrowhead) in left kidney. **B**, DECT image shows properties similar to those of calcium in bone, which enables confident diagnosis of calcium-based stone (e.g., calcium oxalate) (arrowhead).

120 kVp. The single-energy output has a twofold increased noise level compared with that of the mixed images. Rescaling the images to represent actual contrast levels, such as those for iodine maps, further increases the noise level. This makes the application of denoising algorithms necessary for images to be displayed at a diagnostic-quality level [46].

Many practices do not perform DECT for large patients (e.g., patients who weigh > 260 pounds [> 118 kg]) because of the additional photon starvation caused by the large circumference [47]. Many applications, however, are viable for obese patients, if imaging is tailored to resolve specific issues (e.g., increasing the amount of contrast material given or adjusting the timing of the injection) [48].

Although attenuation values measured on VMIs are relatively similar to those seen on single-energy CT of the soft tissues, they are less accurate for high-attenuation material such as bone or vividly enhancing structures like the aorta, showing measurements lower than those seen on a higher-energy, single-energy CT image [49].

The clinical DECT imaging workflow varies widely between institutions [50] and can result in more time being required for the technologist to perform DECT compared with single-energy CT, especially if additional reconstructions or postprocessing are required.

Similarly, the potentially large number of image series provided for the radiolo-

gist to review in the PACS can increase the workload in an already busy clinical environment. DECT, however, might be beneficial in the longer term, if patient recalls and additional examinations can be avoided. This requires stringent protocol implementation and education of both technologists and radiologists regarding the most efficient and beneficial workflows.

## Conclusion

DECT is based on complex physics concepts but can be a very useful tool in the clinical evaluation of patients, adding value to CT and possibly avoiding additional imaging. Several challenges exist in the application of DECT, but most of them can be overcome by applying an optimized technique and implementing stringent acquisition and reading workflows.

## Acknowledgment

We thank Susan Whitney for her help identifying images to be considered candidates for inclusion in this chapter.

## REFERENCES

- Hounsfield GN. Computerized transverse axial scanning (tomography). 1. Description of system. *Br J Radiol* 1973; 46:1016–1022
- Chiro GD, Brooks RA, Kessler RM, et al. Tissue signatures with dual-energy computed tomography. *Radiology* 1979; 131:521–523
- Brody WR, Cassel DM, Sommer FG, et al. Dual-energy projection radiography: initial clinical experience. *AJR* 1981; 137:201–205
- Kelcz F, Joseph PM, Hilal SK. Noise considerations in dual energy CT scanning. *Med Phys* 1979; 6:418–425
- Patino M, Prochowski A, Agrawal MD, et al. Ma-

terial separation using dual-energy CT: current and emerging applications. *RadioGraphics* 2016; 36:1087–1105

- Albrecht MH, Vogl TJ, Martin SS, et al. Review of clinical applications for virtual monoenergetic dual-energy CT. *Radiology* 2019; 293:260–271
- Toia GV, Hartman JB, Sahani DV, Mileto A. Dual-energy CT in the inpatient setting. In: Bhosale P, Marin D, Morgan D, eds. *Practical dual-energy CT throughout the body—a busy radiologist's primer*. Leesburg, VA: American Roentgen Ray Society, 2021:189–195
- Hojjati M, Van Hedent S, Rassouli N, et al. Quality of routine diagnostic abdominal images generated from a novel detector-based spectral CT scanner: a technical report on a phantom and clinical study. *Abdom Radiol (NY)* 2017; 42:2752–2759
- Yuan R, Shuman WP, Earls JP, et al. Reduced iodine load at CT pulmonary angiography with dual-energy monochromatic imaging: comparison with standard CT pulmonary angiography—a prospective randomized trial. *Radiology* 2012; 262:290–297
- Bamberg F, Dierks A, Nikolaou K, Reiser MF, Becker CR, Johnson TR. Metal artifact reduction by dual energy computed tomography using monoenergetic extrapolation. *Eur Radiol* 2011; 21:1424–1429
- Jacobsen MC, Schellingerhout D, Wood CA, et al. Intermanufacturer comparison of dual-energy CT iodine quantification and monochromatic attenuation: a phantom study. *Radiology* 2018; 287:224–234
- Rajiah P, Sundaram M, Subhas N. Dual-energy CT in musculoskeletal imaging: what is the role beyond gout? *AJR* 2019; 213:493–505
- Yu Z, Mao T, Xu Y, et al. Diagnostic accuracy of dual-energy CT in gout: a systematic review and meta-analysis. *Skeletal Radiol* 2018; 47:1587–1593
- Wu H, Zhang G, Shi L, et al. Axial spondyloarthritis: dual-energy virtual noncalcium CT in the detection of bone marrow edema in the sacroiliac joints. *Radiology* 2019; 290:157–164
- Kosmala A, Weng AM, Heidemeier A, et al. Multiple myeloma and dual-energy CT: diagnostic accuracy of virtual noncalcium technique for detection of bone marrow infiltration of the spine and pelvis. *Radiology* 2018; 286:205–213
- Deng K, Sun C, Liu C, Ma R. Initial experience with visualizing hand and foot tendons by dual-energy computed tomography. *Clin Imaging* 2009; 33:384–389
- Cavallo AU, Patterson AJ, Thomas R, et al. Low dose contrast CT for transcatheter aortic valve replacement assessment: results from the prospective SPECTACULAR study (spectral CT assessment prior to TAVR). *J Cardiovasc Comput Tomogr* 2020; 14:68–74
- Zhao LQ, He W, Li JY, Chen JH, Wang KY, Tan L. Improving image quality in portal venography with spectral CT imaging. *Eur J Radiol* 2012; 81:1677–1681
- Godoy MC, Naidich DP, Marchiori E, et al. Single-acquisition dual-energy multidetector computed tomography: analysis of vascular enhancement and postprocessing techniques for evaluating the thoracic aorta. *J Comput Assist Tomogr* 2010; 34:670–677
- Wortman JR, Uyeda JW, Fulwadhva UP, Sodickson AD. Dual-energy CT for abdominal and pelvic trauma. *RadioGraphics* 2018; 38:586–602
- Fulwadhva UP, Wortman JR, Sodickson AD. Use of dual-energy CT and iodine maps in evaluation of bowel disease. *RadioGraphics* 2016; 36:393–406
- Ameli-Renani S, Rahman F, Nair A, et al. Dual-energy CT for imaging of pulmonary hypertension: challenges and opportunities. *RadioGraphics* 2014; 34:1769–1790
- Schwartz FR, Tailor T, Gaca JG, et al. Impact of dual

- energy cardiac CT for metal artefact reduction post aortic valve replacement. *Eur J Radiol* 2020; 129:109135
24. Mangold S, Cannaó PM, Schoepf UJ, et al. Impact of an advanced image-based monoenergetic reconstruction algorithm on coronary stent visualization using third generation dual-source dual-energy CT: a phantom study. *Eur Radiol* 2016; 26:1871–1878
  25. Ruzsics B, Schwarz F, Schoepf UJ, et al. Comparison of dual-energy computed tomography of the heart with single photon emission computed tomography for assessment of coronary artery stenosis and of the myocardial blood supply. *Am J Cardiol* 2009; 104:318–326
  26. Obaid DR, Calvert PA, Gopalan D, et al. Dual-energy computed tomography imaging to determine atherosclerotic plaque composition: a prospective study with tissue validation. *J Cardiovasc Comput Tomogr* 2014; 8:230–237
  27. Patel BN, Thomas JV, Lockhart ME, Berland LL, Morgan DE. Single-source dual-energy spectral multidetector CT of pancreatic adenocarcinoma: optimization of energy level viewing significantly increases lesion contrast. *Clin Radiol* 2013; 68:148–154
  28. Shuman WP, Green DE, Busey JM, et al. Dual-energy liver CT: effect of monochromatic imaging on lesion detection, conspicuity, and contrast-to-noise ratio of hypervascular lesions on late arterial phase. *AJR* 2014; 203:601–606
  29. Patel BN, Vernuccio F, Meyer M, et al. Dual-energy CT material density iodine quantification for distinguishing vascular from nonvascular renal lesions: normalization reduces intermanufacturer threshold variability. *AJR* 2019; 212:366–376
  30. Gnannt R, Fischer M, Goetti R, Karlo C, Leschka S, Alkadhi H. Dual-energy CT for characterization of the incidental adrenal mass: preliminary observations. *AJR* 2012; 198:138–144
  31. Elbanna KY, Mohammed MF, Chahal T, et al. Dual-energy CT in differentiating nonperforated gangrenous appendicitis from uncomplicated appendicitis. *AJR* 2018; 211:776–782
  32. Ratanaprasatporn L, Uyeda JW, Wortman JR, Richardson I, Sodickson AD. Multimodality imaging, including dual-energy CT, in the evaluation of gallbladder disease. *RadioGraphics* 2018; 38:75–89
  33. Boll DT, Patil NA, Paulson EK, et al. Renal stone assessment with dual-energy multidetector CT and advanced postprocessing techniques: improved characterization of renal stone composition—pilot study. *Radiology* 2009; 250:813–820
  34. Werner S, Krauss B, Haberland U, et al. Dual-energy CT for liver iron quantification in patients with haematological disorders. *Eur Radiol* 2019; 29:2868–2877
  35. Tsai YS, Chen JS, Wang CK, et al. Quantitative assessment of iron in heart and liver phantoms using dual-energy computed tomography. *Exp Ther Med* 2014; 8:907–912
  36. Nicolaou S, Liang T, Murphy DT, Korzan JR, Ouellette H, Munk P. Dual-energy CT: a promising new technique for assessment of the musculoskeletal system. *AJR* 2012; 199:578–586
  37. Cai W, Kim SH, Lee J-G, Yoshida H. Informatics in radiology: dual-energy electronic cleansing for fecal-tagging CT colonography. *RadioGraphics* 2013; 33:891–912
  38. Walstra FE, Hickle J, Duggan P, et al. Top-ten tips for dual-energy CT in MSK radiology. *Semin Musculoskelet Radiol* 2019; 23:392–404
  39. Mallinson PI, Coupal T, Reisinger C, et al. Artifacts in dual-energy CT gout protocol: a review of 50 suspected cases with an artifact identification guide. *AJR* 2014; 203:[web]W103–W109
  40. Fischer MA, Gnannt R, Raptis D, et al. Quantification of liver fat in the presence of iron and iodine: an ex-vivo dual-energy CT study. *Invest Radiol* 2011; 46:351–358
  41. Walter D, Tkaczyk E, Wu X. Accuracy and precision of dual energy CT imaging for the quantification of tissue fat content. *Medical imaging 2006: physics of medical imaging—proceedings of SPIE*, vol. 6142. Bellingham, WA: SPIE, 2006: 654669
  42. Petritsch B, Kosmala A, Weng AM, et al. Vertebral compression fractures: third-generation dual-energy CT for detection of bone marrow edema at visual and quantitative analyses. *Radiology* 2017; 284:161–168
  43. Andreini D, Pontone G, Mushtaq S, et al. Diagnostic accuracy of rapid kilovolt peak-switching dual-energy CT coronary angiography in patients with a high calcium score. *JACC Cardiovasc Imaging* 2015; 8:746–748
  44. Wittram C, Maher MM, Yoo AJ, Kalra MK, Shepard JA, McLoud TC. CT angiography of pulmonary embolism: diagnostic criteria and causes of misdiagnosis. *RadioGraphics* 2004; 24:1219–1238
  45. Johnson TRC. Dual-energy CT: general principles. *AJR* 2012; 199:53–58
  46. Grant KL, Flohr TG, Krauss B, Sedlmair M, Thomas C, Schmidt B. Assessment of an advanced image-based technique to calculate virtual monoenergetic computed tomographic images from a dual-energy examination to improve contrast-to-noise ratio in examinations using iodinated contrast media. *Invest Radiol* 2014; 49:586–592
  47. Megibow AJ, Sahani D. Best practice: implementation and use of abdominal dual-energy CT in routine patient care. *AJR* 2012; 199:571–577
  48. Kordbacheh H, Baliyan V, Uppot RN, Eisner BH, Sahani DV, Kambadakone AR. Dual-source dual-energy CT in detection and characterization of urinary stones in patients with large body habitus: observations in a large cohort. *AJR* 2019; 212:796–801
  49. Sellaer T, Noël PB, Patino M, et al. Dual-energy CT: a phantom comparison of different platforms for abdominal imaging. *Eur Radiol* 2018; 28:2745–2755
  50. Patel BN, Alexander L, Allen B, et al. Dual-energy CT workflow: multi-institutional consensus on standardization of abdominopelvic MDCT protocols. *Abdom Radiol (NY)* 2017; 42:676–687